

# Learning Transferable Deep Models for Land-Use Classification with High-Resolution Remote Sensing Images\*

Xin-Yi Tong<sup>1</sup>, Gui-Song Xia<sup>1</sup>, Qikai Lu<sup>2</sup>, Huanfeng Shen<sup>3</sup>, Shengyang Li<sup>4</sup>,  
Shucheng You<sup>5</sup>, Liangpei Zhang<sup>1</sup>

<sup>1</sup>*State Key Laboratory LIESMARS, Wuhan University, China.*

<sup>2</sup>*Electronic Information School, Wuhan University, China.*

<sup>3</sup>*School of Resource and Environmental Sciences, Wuhan University, China.*

<sup>4</sup>*Key Laboratory of Space Utilization, Tech. & Eng. Center for Space Utilization,  
Chinese Academy of Sciences, China.*

<sup>5</sup>*Remote Sensing Department, China Land Survey and Planning Institute, China.*

July 12, 2021

## Abstract

In recent years, large amount of high spatial-resolution remote sensing (HRRS) images are available for land-use mapping. However, due to the complex information brought by the increased spatial resolution and the data disturbances caused by different conditions of image acquisition, it is often difficult to find an efficient method for achieving accurate land-use classification with heterogeneous and high-resolution remote sensing images. In this paper, we propose a scheme to learn transferable deep models for land-use classification with HRRS images. The main idea is to rely on deep neural networks for presenting the semantic information contained in different types of land-uses and propose a pseudo-labeling and sample selection scheme for improving the transferability of deep models. More precisely, a deep Convolutional Neural Networks (CNNs) is first pre-trained with a well-annotated land-use dataset, referred to as the *source data*. Then, given a *target image* with no labels, the pre-trained CNN model is utilized to classify the image in a patch-wise manner. The patches with high classification probability are assigned with pseudo-labels and employed as the queries to retrieve related samples from the source data. The pseudo-labels confirmed with the retrieved results are regarded as supervised information for fine-tuning the pre-trained deep model. In order to obtain a pixel-wise land-use classification with the target image, we rely on the fine-tuned CNN and develop a hybrid classification by combining patch-wise classification and hierarchical segmentation. In addition, we create a large-scale land-use dataset containing 150 Gaofen-2 satellite images for CNN pre-training. Experiments on multi-source HRRS images, including Gaofen-2, Gaofen-1, Jilin-1, Ziyuan-3, and Google Earth images, show encouraging results and demonstrate the efficiency of the proposed scheme for learning transferable deep models for land-use classification with HRRS images.

## 1 Introduction

Land-use classification with remote sensing (RS) images plays an important role in many applications such as land resource management, urban planning, precision agriculture, and environmental protection [1–6]. In

---

\*A website is available at <http://captain.whu.edu.cn/GID/>

recent years, high-resolution remote sensing (HRRS) images are increasingly available. Meanwhile, multi-source and multi-temporal RS images can be obtained over different geographical areas [7]. Such large amount of heterogeneous HRRS images provide detailed information of the land surface, and therefore open new avenues for large-coverage and multi-temporal land-use mapping. However, the rich details of objects emerging in HRRS images, such as the geometrical shape and structural content of objects, bring more challenges to land-use classification [8]. Furthermore, diverse imaging conditions usually lead to photographic distortion, variations in scales and changes of illuminations in RS images, which often seriously reduces the separability among different classes [9]. Due to these influences, optimal classification models learned from certain annotated images always quickly lose their efficiency on new images captured by different sensors or by the same sensors but from different geo-locations. Therefore, it is intractable to find an efficient and accurate land-use classification method for HRRS images with large diversities.

## 1.1 Motivation and objective

In the literature, in order to characterize the image content of different land-use categories, many methods investigated the use of spectral and spectral-spatial features to interpret RS images [10–17]. However, due to the detailed and structural information brought by the gradually increased spatial resolution, the spectral and spectral-spatial features have difficulty in describing the semantic information contained in the images [18–21], which are often essential in depicting land-use categories in HRRS images. Recently, it has been reported that effective characterization of semantic information in HRRS images can largely improve the classification performance [22–24]. Among them, deep Convolutional Neural Networks (CNNs) have been drawn much attention in the understanding of HRRS images [25, 26], mainly because of their strong capability to depict high-level and semantic aspects of images [27, 28]. Currently, various deep models have been adopted to cope with challenging issues in RS image understanding, including *e.g.* scene classification [25, 29], object detection [30], image retrieval [31–33], as well as land-use classification [34–39].

In this paper, we target to develop a transferable deep model for land-use classification with multi-source HRRS images, which is mainly motivated by following two aspects.

- *The inadequate transferability of deep learning models:* Due to the diverse distributions of objects and spectral shifts caused by the different acquisition conditions of images, deep models trained on a certain set of annotated RS images may not be effective when dealing with images acquired by different sensors or from different geo-locations [40]. In order to obtain satisfactory land-use classification on a RS image of interest, referred as the target image, new specific annotated samples closely related to it are often necessary for model fine-tuning [37]. Nevertheless, considering that manual annotation requires high labor intensity and is often time-consuming, it is infeasible to label sufficient samples for continuously accumulated multi-source RS images [41, 42].
- *The lack of well-annotated large-scale land-use dataset:* The identification capability of CNN models relies heavily on the quality and quantity of the training data [43]. Up to now, several land-use datasets have been proposed in the community, and have advanced a lot deep-learning-based land-use classification approaches [44–46]. However, the geographic areas covered by most of existing land-use datasets [44, 46, 47] do not exceed  $10km^2$  and somewhat similar in geographic distributions [48]. The lack of variations in geographic distributions of annotated HRRS images may cause overfitting in learning deep models and limit the generalization ability of learned models. Overall, the insufficient or unqualified training data restrict the efficiency and availability of deep models for HRRS images.

## 1.2 Related work

Land-use classification with RS images aims to associating each pixel in a RS image with a pre-defined land-use label. To this end, classification approaches using spectral information have been intensively studied. These methods can interpret RS images using the spectral features of individual pixels [10–12], but their

performances are often heavily affected by intra-class spectral variations and noises [49–51]. More recently, the spatial information has been taken into consideration for land-use classification [13–17]. Spectral-spatial classification incorporates spatial contextual information, such as texture [52–54], shape [55], and structure features [56, 57], to improve the separability of different categories in the feature space. It has been reported that spectral-spatial approaches can effectively boost the categorization accuracy compared with the methods using spectral features [58–61]. However, with the spatial-resolution of RS image improving, rather than discriminating in spectral or spectral-spatial information of local pixels, land-use types are more categorized in their semantic meanings [22, 24]

Recently, deep neural network models have been intensively studied to address the problem of land-use classification and reported impressive performances, see *e.g.* [34–36, 62–64]. In contrast with conventional methods that employ spectral or spectral-spatial features for land-use description, a significant advantage of deep learning approaches is that they are able to adaptively learn discriminative features from images [28]. The land-use classification approaches that utilize deep features treat CNN models as feature extractors and employ conventional classifiers [34–36, 62–64], such as support vector machine (SVM) and logistic regression, for classification. These methods are suitable for classification tasks of small amount of data. As an alternative, end-to-end CNN models are adopted to interpret RS images [37–39, 65, 66]. End-to-end CNN models, such as Fully Convolutional Networks (FCN) [37], conduct dense land-use labeling for RS images without using additional classifiers or post-processing. Although, compared with using deep features, end-to-end CNN models are more efficiency for classification, the down- and up-sampling processes in the end-to-end models often lead to loss of spatial information in the classification map [66].

### 1.3 Contributions

In this paper, we propose a land-use classification algorithm, which can be transferred to interpret multi-source HRRS images without the need of specialized sample annotation. In our classification process, a patch-wise classification is initially conducted on the image relying on the multi-scale contextual information extracted by CNN. Then, a hierarchical segmentation is used for obtaining the object boundary information, which is integrated into the patch-wise classification map for accurate results. In order to acquire high-performance classification models for multi-source HRRS images, we propose to train specialized CNN with samples of each target image. Considering that the textures and structures of the objects are not affected by the spectral shifts, we use semantic information extracted by CNN to automatically mine training samples. Concretely, unlabeled samples in the target image are identified by a CNN model pre-trained on an annotated HRRS dataset, which is referred to as the source data. A subset of them with high classification probability are assigned with pseudo-labels and employed to retrieve similar samples from the source data. Finally, the returned results are used to determine whether the pseudo-labels are reliable for fine-tuning. Specifically, for pre-training CNN models, we annotate 150 Gaofen-2 satellite images to construct a land-use classification dataset, which is named after *Gaofen Image Dataset* (GID).

In summary, the contributions of this paper are as follows:

- We propose a scheme to learn transferable deep models, which enables one to achieve land-use classification by using multi-source RS images with high spatial resolution. The proposed algorithm can simultaneously extract accurate category and boundary information of the ground objects. In addition, it requires no new labeled samples when dealing with the target images. Experiments conducted on multi-source HRRS images, including Gaofen-2, Gaofen-1, Jilin-1, Ziyuan-3, and Google Earth images obtain promising results and demonstrate the efficiency of the proposed scheme.
- We present a large-scale land-use classification dataset, namely GID, which is consist of 150 high-resolution Gaofen-2 images and covers areas more than 50,000  $km^2$  in China. To our knowledge, GID is the first and largest well-annotated land-use classification dataset with high-resolution remote sensing images up to 4 meters. It can provide the research community a high-quality dataset to advance land-use classification with HRRS images, *like* Gaofen-2 imagery.

A preliminary version of this work was presented in [67].

## 1.4 Organization of this paper

The remainder of the paper is organized as follows: In Section 2, the introduction of our land-use classification algorithm is presented. In Section 3, the details and properties of GID coupled with other examined images are described. We present and discuss the results of experiments in Section 4. Finally, we conclude our work in Section 5.

## 2 Methodology

In order to efficiently classify multi-source HRRS images, we propose a transferable land-use classification algorithm that needs no manual annotation of samples. Assume that there is a well-annotated large-scale dataset, which will be introduced in Section 3, and a newly acquired image without labeling information. We define two domains, called source domain  $\mathbf{D}_S$  and target domain  $\mathbf{D}_T$  that are separately associated with the labeled and unlabeled images. Our aim is to exploit the information learned from the source domain  $\mathbf{D}_S$  to conduct classification in the target domain  $\mathbf{D}_T$ .

Firstly, we use  $\mathbf{D}_S$  to pre-train a deep model specific to RS domain, which is presented in Section 2.1. Given a target image  $\mathbf{I}_T$  belonging to  $\mathbf{D}_T$ , we divide it into patches  $\mathbf{U} = \{\mathbf{x}_i\}_{i=1}^I$  with non-overlapping grid partition. Our method automatically searches reliable training samples from  $\mathbf{U}$  to learn transferable deep model for  $\mathbf{I}_T$ , as introduced in Section 2.2. Subsequently, we utilize the fine-tuned deep model to classify  $\mathbf{x}_i$  for all  $i \in \{1, \dots, I\}$ . Our classification scenario combines patch-wise categorization and object-based voting, which is described in Section 2.3.

### 2.1 Learning deep model for land-use classification

We employ 50-layer Residual Network (ResNet-50) [68] as the classifier in our work. ResNet-50 consists of 16 bottleneck structures, each of which has 3 convolutional layers that constitute a shortcut connection. The first convolutional layer of the overall model is followed by a max pooling layer. An average pooling layer, a full-connected layer, and a softmax layer are subsequent to the last convolutional layer. The structures of residual learning and shortcut mapping can relieve the problem of gradient disappearance. Compared with the common CNN models [27, 69–71], ResNets are easier to train when the network architectures are extremely deep.

In order to pre-train a CNN model with strong discrimination ability for HRRS images, we construct a large-scale land-use dataset, Gaofen Image Dataset (GID), which will be represent in Section 3. GID is first randomly divided into 120 training images and 30 test images, of which the training images are referred to as  $\mathbf{D}_S$ . Patches of size  $56 \times 56$  are randomly sampled on the training images. If more than 80% pixels in the patch are covered by the same category, the center pixel of this patch is considered as a reference pixel. To exploit the multi-scale contextual information, the size of the patches centered on the reference pixels are set as:  $56 \times 56$ ,  $112 \times 112$ , and  $224 \times 224$  pixels. For each of the five categories in GID, 10,000 sampling pixels are selected. Thus, a total of 150,000 patches are collected to pre-train ResNet-50 model. Image augmentation strategies [27] are adopted to avoid overfitting.

For CNN model training, the parameters of ResNet-50 are initialized with ImageNet. Since the category numbers of ImageNet and GID are different, a 5-dimensional softmax layer is used instead of the 1000-dimensional softmax layer in ResNet-50. 1000 and 5 are the class numbers of ImageNet and GID, respectively. The new softmax layer is initialized by Gaussian distribution. The last three bottlenecks and softmax layer of ResNet-50 are trained. The hyper-parameters for training are set as follows: batch size is 32, epoch number is 15, momentum value is 0.9, and initial learning rate is 0.1. When the error rate stops decreasing, we divide the learning rate by 10 and use the new value to update the parameters. The learning rate reduces three times until ResNet-50 model is converged.

## 2.2 Learning transferable model for multi-source images

Although CNNs have a certain degree of generalization ability, they are unable to achieve satisfactory classification results on multi-source RS images because of dramatic changes in acquisition conditions. In order to transfer CNN models for classifying RS images acquired under different conditions, we introduce an automatic training sample acquisition scheme that requires no manual operations.

As shown in Fig. 1, the proposed scheme is divided into two stages: pseudo-label assignment and relevant sample retrieval, which are presented in Section 2.2.1 and Section 2.2.2, respectively. Category predictions and deep features generated by CNN are used to search target samples that possess similar characteristics to the source domain. These relevant samples and their corresponding category predictions, which are referred to as pseudo-labels, are used for CNN model fine-tuning.

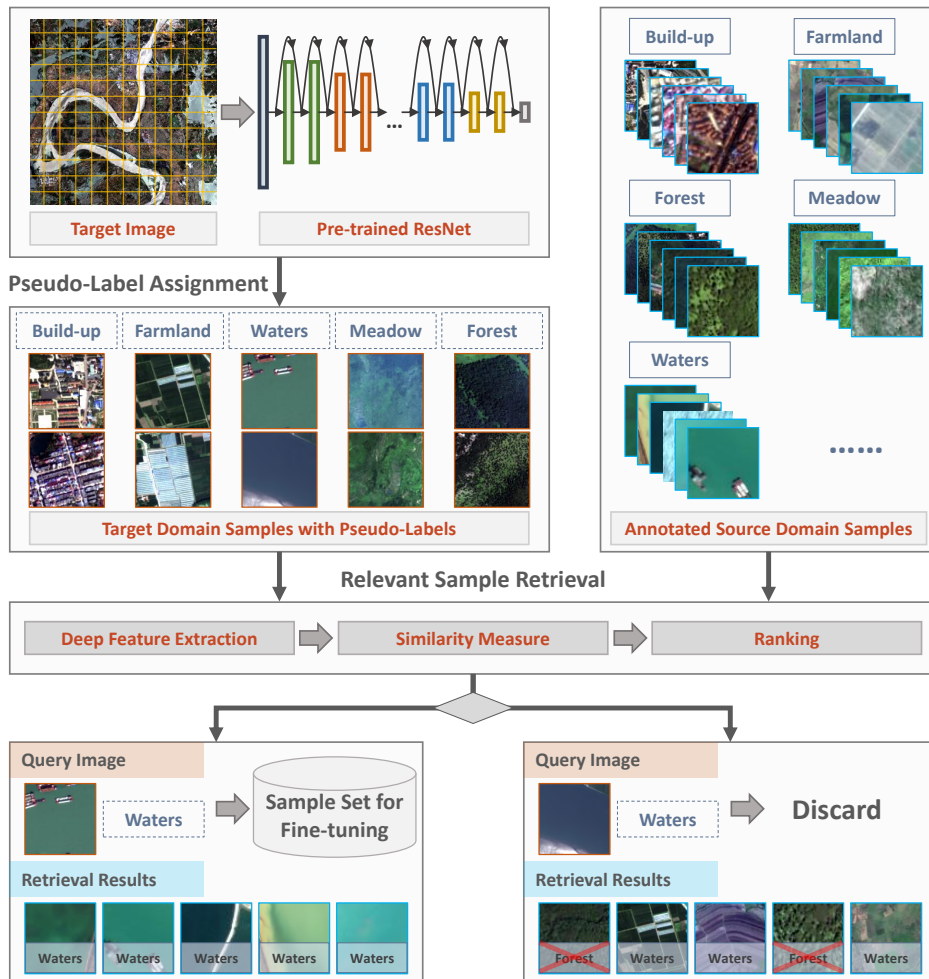


Figure 1: Sample selection for model fine-tuning.

### 2.2.1 Pseudo-label assignment

Given the patch set  $\mathbf{U} = \{\mathbf{x}_i\}_{i=1}^I$  of a target image  $\mathbf{I}_T$ , we input each patch  $\mathbf{x}_i$  to ResNet-50 that has been pre-trained on  $\mathcal{D}_S$ . The output vectors of softmax layer form a set  $\mathbf{F} = \{\mathbf{p}_i\}_{i=1}^I$ , where:

$$\mathbf{p}_i = \{p_{i,1}, p_{i,2}, \dots, p_{i,K}\}, \mathbf{p}_i \in \mathbb{R}^K \quad (1)$$

where  $p_{i,k}$  represents the probability that patch  $\mathbf{x}_i$  belongs to class  $k$ ,  $k \in \{1, \dots, K\}$ , and  $K$  is the total number of classes.  $\mathbf{p}_i$  is the predicted classification probability vector, of which the highest probability value is  $h = \max_{k \in \{1, \dots, K\}} p_{i,k}$ .

Since CNN model has strong discriminating ability, we use the probability value to determine whether a sample is associated with a label. If the value of  $h$  is greater than or equal to a threshold  $\sigma$ , the patch  $\mathbf{x}_i$  is reserved and assigned with a predicted category  $l_i$ . Otherwise,  $\mathbf{x}_i$  is removed from  $\mathbf{U}$ .  $l_i$  corresponds to the category represented by  $h$  and is referred to as a pseudo-label. The threshold  $\sigma$  is set to be 0.8. After removing all patches with low classification confidence from  $\mathbf{U}$ , the remaining samples form a new set  $\mathbf{U}_1$ .

### 2.2.2 Relevant sample retrieval

Assume that there are  $J$  candidates remaining in the set  $\mathbf{U}_1$ ,  $\mathbf{U}_1 = \{\mathbf{x}_j\}_{j=1}^J$ . For the patch  $\mathbf{x}_j$ , the information entropy  $E_j$  is calculated to measure its classification uncertainty:

$$E_j = - \sum_{k=1}^K p_{j,k} \cdot \log(p_{j,k}) \quad (2)$$

where  $p_{j,k}$  represents the probability that patch  $\mathbf{x}_j$  belongs to class  $k$ .

The patches with higher information entropy are considered as valuable training samples, hence we treat them as preferred candidates. The patches in  $\mathbf{U}_1$  are then sorted according to the descending order of  $E_j$  value, forming a sample set  $\mathbf{U}_2 = \{\hat{\mathbf{x}}_j\}_{j=1}^J$ . Considering that data with low information entropy provides insufficient information, we only use the top  $\mu$  candidates of each category in the set  $\mathbf{U}_2$  to perform retrieval as follows. We fix  $\mu$  as 4000.

Given a patch  $\hat{\mathbf{x}}_j$  that possesses the pseudo-label  $\hat{l}_j$ , we take it as a query image and retrieve its similar samples from the source domain  $\mathbf{D}_S$ . We use the deep features extracted from full-connected layer of the pre-trained ResNet-50 for retrieval. And the feature vectors are compressed by principal component analysis (PCA) for higher calculation efficiency. The similarities between  $\hat{\mathbf{x}}_j$  and the source domain samples are measured by the Euclidean distance.

Then, we use the existing labels of the source domain to determine the confidence of the pseudo-labels. If the top  $\delta$  retrieved results from the source domain have the same label  $g$ , and  $g$  is the same as the pseudo-label  $\hat{l}_j$  of the query patch  $\hat{\mathbf{x}}_j$  (*i.e.*  $\hat{l}_j = g$ ),  $\hat{\mathbf{x}}_j$  is considered to be a relevant sample. Otherwise,  $\hat{\mathbf{x}}_j$  is removed from the set  $\mathbf{U}_2$ .  $\delta$  is set to be 5. After sample screening, the remainders of  $\mathbf{U}_2$  form a new target domain set  $\mathbf{U}_{tg}$ . Finally, the image patches along with their corresponding pseudo-labels in the set  $\mathbf{U}_{tg}$  are used to fine-tune a CNN model that is specific to the target image.

## 2.3 A hybrid land-use classification algorithm

Land-use classification aims to assign pixels in a RS image with land-use category labels. Both the category and boundary information of the ground objects is essential for accurate classification results. We therefore propose a hybrid algorithm, which combines patch-wise classification and hierarchical segmentation through a majority voting strategy, as shown in Fig. 2.

### 2.3.1 Patch-wise classification

Since the ground objects show different characteristics in different spatial resolutions, it is difficult to capture sufficient information of objects from the single-scale observation field. In order to exploit the attributes of the objects and their spatial distributions, we propose to utilize multi-scale contextual information for classification, which is illustrated in Fig. 3.

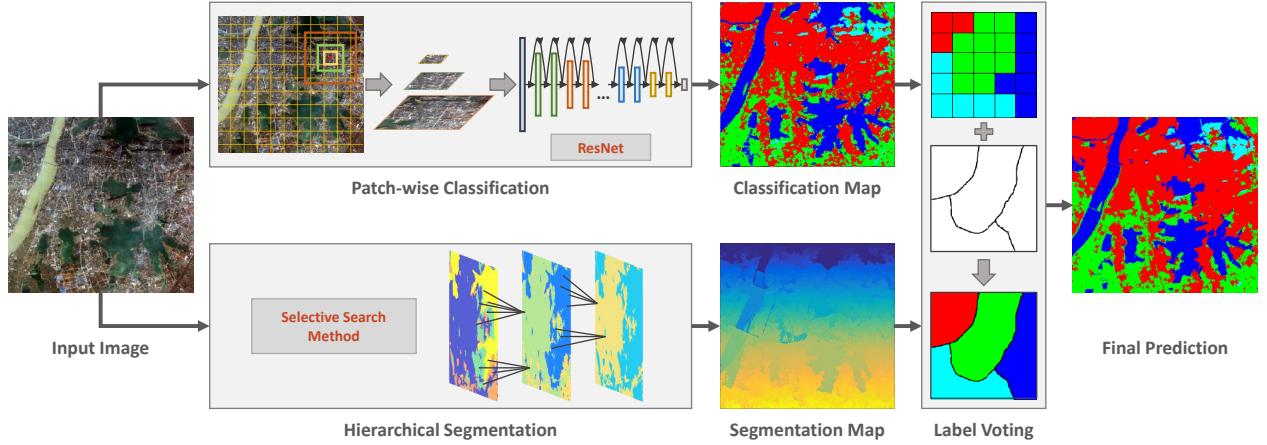


Figure 2: The proposed land-use classification approach.

The target image  $\mathbf{I}_T$  is partitioned into non-overlapping patches  $\mathbf{U} = \{\mathbf{x}_i\}_{i=1}^J$  by grid with the size of  $s_1 \times s_1$  pixels ( $s_1$  is the minimum value in the succession of scales). For each patch  $\mathbf{x}_i$ , its center pixel is regarded as a reference pixel  $\mathbf{z}$ . Around  $\mathbf{z}$ , a series of patches with sizes of  $s_2 \times s_2, \dots, s_N \times s_N$  pixels are sampled, so that each reference pixel possesses  $N$  multi-scale samples. Such multi-scale patches are input to the fine-tuned ResNet-50 model. After forward propagation in ResNet-50, the classification probability vector  $\mathbf{p}_{s_n}(\mathbf{z})$  of scale  $s_n$  at pixel  $\mathbf{z}$  is obtained from softmax layer:

$$\mathbf{p}_{s_n}(\mathbf{z}) = \{p_{s_n,1}(\mathbf{z}), p_{s_n,2}(\mathbf{z}), \dots, p_{s_n,K}(\mathbf{z})\}, \mathbf{p}_{s_n}(\mathbf{z}) \in \mathbb{R}^K \quad (3)$$

where  $n \in \{1, \dots, N\}$ ,  $p_{s_n,k}(\mathbf{z})$  represents the probability that  $\mathbf{z}$  belongs to class  $k$  at the  $n$ -th scale.

Contextual information of multi-scale patches is aggregated using a weighted fusion strategy. The specificity measure [72], which describes the certainty of classification result, is employed as the weight:

$$W_{s_n}(\mathbf{z}) = \sum_{k=1}^{K-1} \frac{1}{k} \cdot (\hat{p}_{s_n,k}(\mathbf{z}) - \hat{p}_{s_n,k+1}(\mathbf{z})) \quad (4)$$

where  $\{\hat{p}_{s_n,1}(\mathbf{z}), \hat{p}_{s_n,2}(\mathbf{z}), \dots, \hat{p}_{s_n,K}(\mathbf{z})\}$  is the descending order of the vector  $\mathbf{p}_{s_n}(\mathbf{z})$ . The value of  $W_{s_n}(\mathbf{z})$  ranges from 0 to 1, and the higher value signifies the higher categorization confidence. The weighted probability  $\tilde{\mathbf{p}}_k(\mathbf{z})$  is expressed as:

$$\tilde{\mathbf{p}}_k(\mathbf{z}) = \frac{\sum_{n=1}^N W_{s_n}(\mathbf{z}) \cdot p_{s_n,k}(\mathbf{z})}{\sum_{n=1}^N W_{s_n}(\mathbf{z})} \quad (5)$$

where  $\tilde{\mathbf{p}}_k(\mathbf{z}) \in [0, 1]$  indicates the probability that the reference pixel  $\mathbf{z}$  belongs to class  $k$ . The aggregated probabilities of all categories can constitute a new classification probability vector. Then the reference pixel  $\mathbf{z}$  is classified as:

$$l(\mathbf{z}) = \arg \max_{k \in \{1, \dots, K\}} \tilde{\mathbf{p}}_k(\mathbf{z}) \quad (6)$$

where  $l(\mathbf{z})$  is the category label of the pixel  $\mathbf{z}$ . Then, we assign the label  $l(\mathbf{z})$  to each pixel in the patch  $\mathbf{x}_i$ . After classifying all the patches in the entire RS image, a patch-wise classification map  $\mathbf{I}_c$  is therefore acquired.

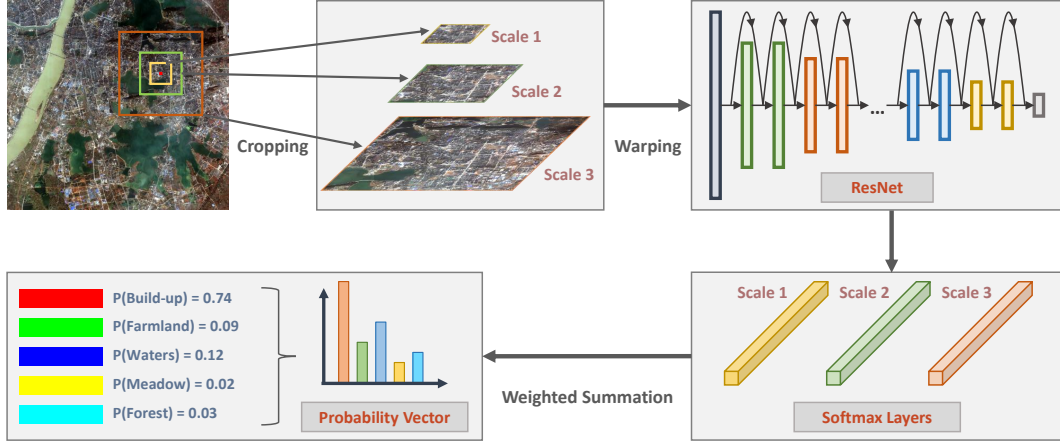


Figure 3: Multi-scale contextual information aggregation.

### 2.3.2 Object-based voting

In order to obtain precise boundary information of the objects, we utilize segmentation map generated by selective search method [73] to refine the preliminary classification map. Selective search is a hierarchical segmentation method. It exploits a graph-based approach [74] to produce a series of initial regions in different color spaces, and then uses the greedy algorithm to iteratively merge small regions. The color, texture, size and fill similarities are employed to control the merging level. Since various image features are considered in the process of initial segmentation and iterative merging, selective search can produce high-quality segmentation results.

After obtaining classification and segmentation maps by patch-wise classification and selective search, we integrate the category and boundary information using a majority voting strategy. Let  $\mathbf{V} = \{\mathbf{y}_f\}_{f=1}^F$  denote the homogeneous regions in the segmentation map  $\mathbf{I}_s$  generated from the target image  $\mathbf{I}_T$ . And  $\hat{\mathbf{y}}_f$  is the corresponding area of  $\mathbf{y}_f$  in the classification map  $\mathbf{I}_c$ . The number of pixels contained by  $\hat{\mathbf{y}}_f$  is  $M = |\mathbf{y}_f|$ , and category label of the  $m$ -th pixel is  $l_m$ ,  $m \in \{1, \dots, M\}$ . Then the number of pixels belonging to each class in  $\hat{\mathbf{y}}_f$  is counted, and the most frequent label  $T(\mathbf{y}_f)$  is assigned to all pixels in  $\mathbf{y}_f$ :

$$T(\mathbf{y}_f) = \arg \max_{r \in \{1, \dots, K\}} \sum_{m=1}^M \text{sign}(l_m = r) \quad (7)$$

where  $\text{sign}(\cdot)$  is an indicator function,  $\text{sign}(\text{true}) = 1$ ,  $\text{sign}(\text{false}) = 0$ , and  $r$  denotes the possible class label. For all segmented objects, the same voting scheme is applied, and the final classification result is then acquired.

## 3 GID: a well-annotated dataset for land-use classification

In this paper, a large-scale land-use dataset containing 150 annotated Gaofen-2 (GF-2) satellite images is constructed. This new dataset, which is named as Gaofen Image Dataset (GID), has superiorities over the existing land-use dataset because of its large coverage, wide distribution, and high spatial resolution. In our work, we utilize GID to pre-train a CNN model with strong generalization ability specific to RS domain. It is worth noting that GID has high intra-class differences and low inter-class diversities. And it can serve as data resource to advance the state-of-the-art in land-use classification task. GID and its reference annotations have been provided online at <http://captain.whu.edu.cn/GID/>.



In addition, in order to validate the transferability of our method on multi-source HRRS images, we annotate high-resolution images acquired by different sensors, including Gaofen-1, Jilin-1, Ziyuan-3 satellite images, and Google Earth images. GID and multi-source images are introduced in Section 3.1 and Section 3.2, respectively.

### 3.1 Gaofen image dataset

#### 3.1.1 Gaofen-2 satellite images

Gaofen-2 (GF-2) is the second satellite of High-definition Earth Observation System (HDEOS) promoted by China National Space Administration (CNSA). Two panchromatic and multispectral (PMS) sensors with spatial resolution of 1 *m* panchromatic (pan)/4 *m* multispectral (MS) are onboard the GF-2 satellite, with a combined swath of 45 *km*.

The multispectral image we used to establish GID provide a spectral range of blue (0.45-0.52  $\mu m$ ), green (0.52-0.59  $\mu m$ ), red (0.63-0.69  $\mu m$ ) and near-infrared (0.77-0.89  $\mu m$ ), and a spatial dimension of  $6908 \times 7300$  pixels covering a geographic area of 506  $km^2$ . GF-2 satellite realizes global observation within 69 days and repeat observations within 5 days, which is only 1/3 of that for Landsat (16 days).

GF-2 images achieve a combination of high spatial resolution and wide field of view, allowing the observation of detailed information over large areas. Since launched in 2014, GF-2 has been made use of for land-use surveys, environmental monitoring, crop estimation, construction planning and other important applications.

#### 3.1.2 Land-use and land cover types

In GID, five representative land-use categories are annotated: *built-up*, *farmland*, *forest*, *meadow*, and *waters*. These land-use categories are labeled with five different colors: red, green, cyan, yellow, and blue, respectively. Areas that do not belong to the above five categories or cannot be artificially recognized are labeled as unknown, which is represented using black color. Fig. 4 shows some samples and their corresponding label masks of GID.

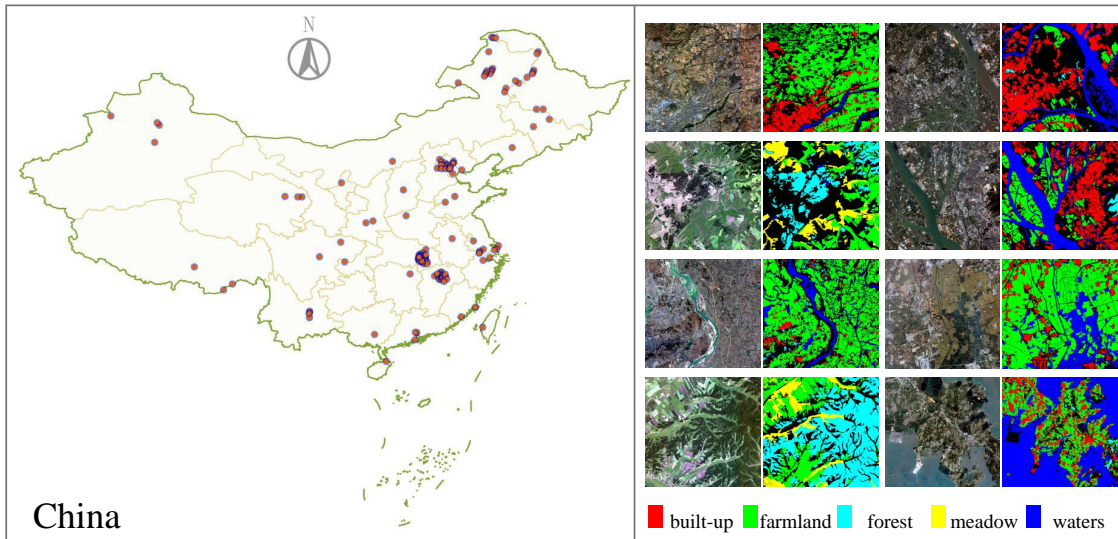


Figure 4: Left: Distribution of the geographical locations of images in GID. Right: Examples of GF-2 images and their corresponding label masks in GID.

### 3.1.3 Dataset properties

GID contains 150 high-quality GF-2 images acquired from more than 60 different cities in China, which is shown in Fig. 4. It is widely distributed over the geographic areas covering more than 50,000  $km^2$ . The acquisition time of GF-2 images in GID is between December 5, 2014 and October 13, 2016. GID has the following properties:

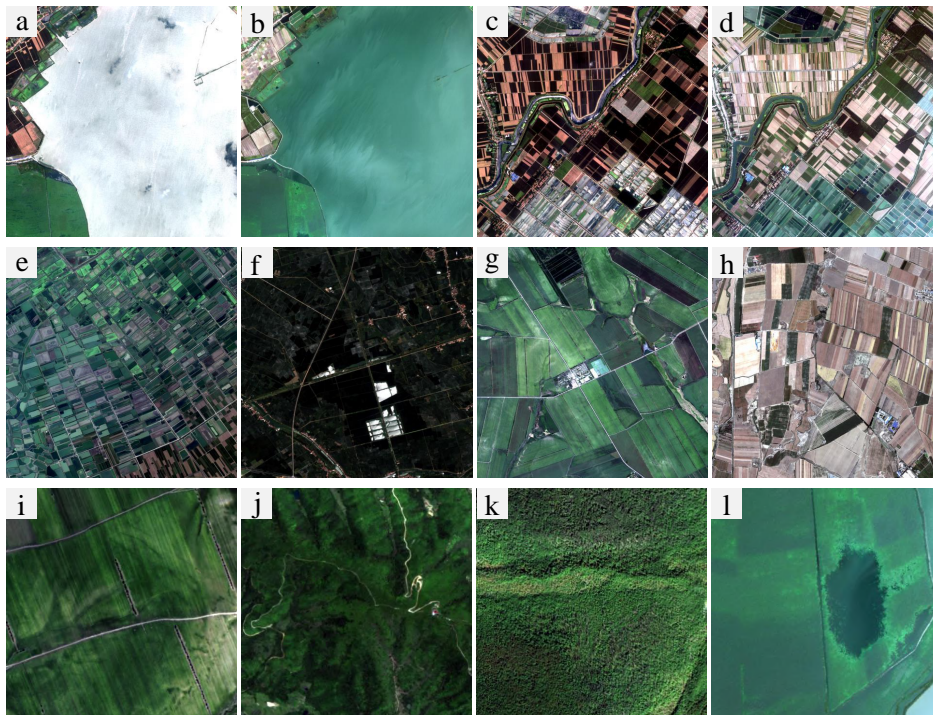


Figure 5: (a)-(d) Multitemporal samples at the same acquisition locations. (e)-(h) Intra-class variations of GID. (i)-(l) Inter-class similarities of GID.

**High intra-class variations:** Due to the different acquisition time and extensive geographical distribution, GID presents rich diversity in spectral response and morphological structure, which greatly increases the intra-class variations. For instance, Fig. 5(a)-(d) illustrate lake and farmland areas around Xiantao, Hubei Province acquired on September 2, 2015 and June 14, 2016 respectively. It can be seen that although the textures and shapes in multitemporal images are almost unchanged, the spectral responses emerge in distinct differences. For another example, Fig. 5(e)-(h) display farmland areas in Jingzhou, Hubei Province, Nanchang, Jiangxi Province, Heihe, Heilongjiang Province, and Changji, Xinjiang Province, respectively. All of the spectral, texture and shape properties appearing in these images are completely diverse.

**Low inter-class separability:** Moreover, because of the influence of natural factors, different land-use categories may appear alike in RS images, which reduces the inter-class separability of GID. For instance, Fig. 5(i)-(l) show farmland in Heihe, Heilongjiang Province, forest in Fuzhou, Jiangxin Province, meadow in Hulun Buir, Inner Mongolia, and eutrophic waters in Xiantao, Hubei Province. Since they are all covered by vegetation, the spectral responses over them are quite similar.

## 3.2 Gaofen-1, Jilin-1, Ziyuan-3, and Google Earth images

Newly acquired RS images may come from different sensors, hence the classification of the multi-source images is of great significance. We also verify the effectiveness of our algorithm on HRRS images captured

by other sensors, including Gaofen-1 (GF-1), Jilin-1 (JL-1), Ziyuan-3 (ZY-3), and Google Earth images. The introduction of these images is as follows.

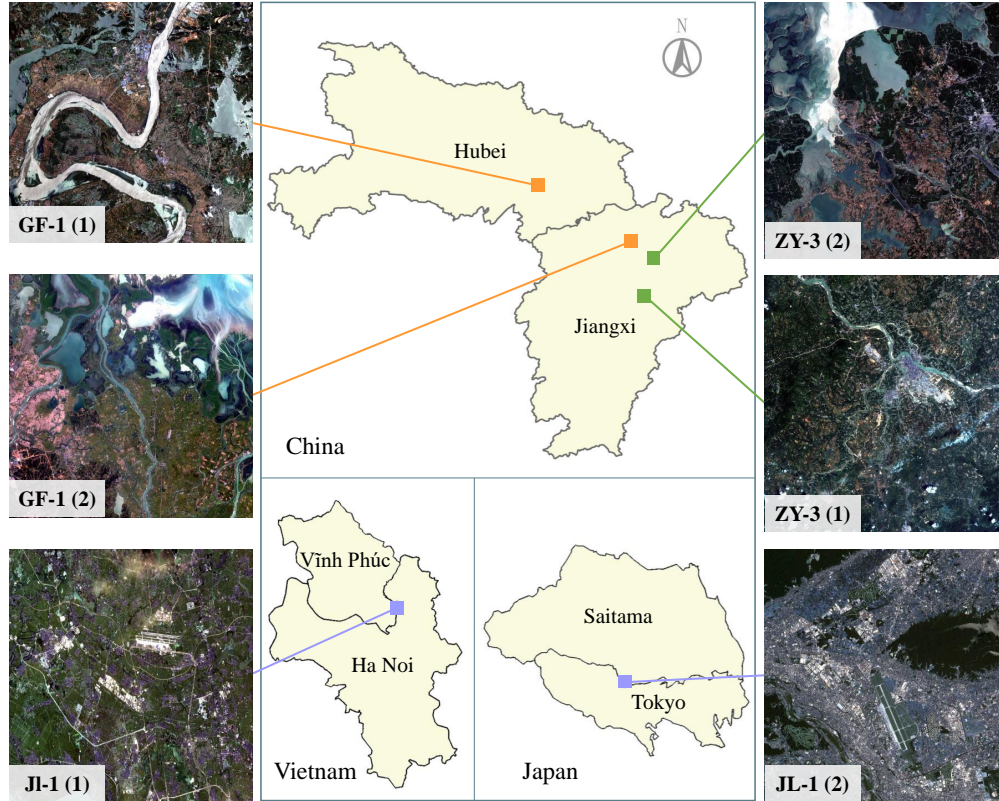


Figure 6: GF-1, JL-1, ZY-3 satellite images and their acquisition locations.

### 3.2.1 Gaofen-1 satellite images

GF-1 satellite configures with two PMS and four wide field of view (WFV) sensors. The resolution of PMS is 2 m pan/8 m MS, and the swath is 60 km. Two GF-1 multispectral images that were captured in Wuhan, Hubei Province on July 25, 2016, and in Jiujiang, Jiangxi Province on October 16, 2015 are employed in the experiments. We denote them as GF-1(1) and GF-1(2), as shown in Fig. 6.

### 3.2.2 Jilin-1 satellite images

The resolution of JL-1 satellite is 0.72 m pan/2.88 m MS, and it has only three bands of red, green, and blue. Two JL-1 multispectral images that were respectively captured around Ha Noi, Vietnam on June 11, 2016, and around Tokyo, Japan on June 3, 2016 are used in the experiments. We denote them as JL-1(1) and JL-1(2), as shown in Fig. 6.

### 3.2.3 Ziyuan-3 satellite images

ZY-3 satellite configures with three panchromatic time delay integration (TDI) charge coupled device (CCD) sensors and a multispectral scanner (MSS). The resolution of MSS is 5.8 m, and the swath is 52 km. Two ZY-3 multispectral images that were respectively captured in Fuzhou, Jiangxi Province on August 28, 2016,

and in Shangrao, Jiangxi Province on August 28, 2016 are utilized in the experiments. We denote them as ZY-3 (1) and ZY-3 (2), as shown in Fig. 6.

### 3.2.4 Google Earth images

To confirm the practicality of our algorithm for application, we conduct land-use classification in Wuhan, Hubei province, China. Google Earth images captured on December 9, 2017 from Wuhan area are utilized. They have the resolution of 4.78 m and contains only three bands of red, green, and blue. We refer to these images as GE-WH, as shown in Fig. 7.

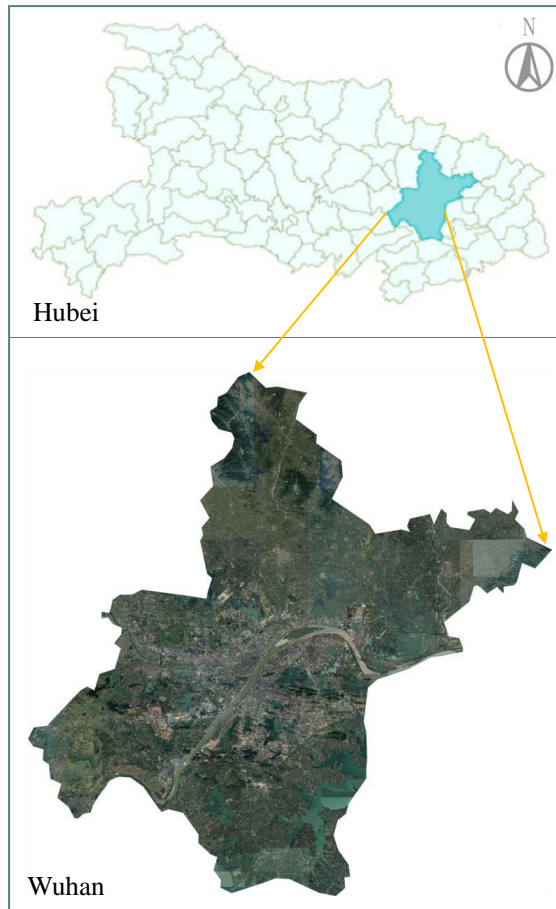


Figure 7: Google Earth image in Wuhan, Hubei province, China.

## 4 Experiments and discussion

We test our algorithm and discuss the experimental results in this section. Two types of land-use classification issues are examined: 1) transferring deep models to classify HRRS images captured with the same sensor and under different conditions, 2) transferring deep models to classify multi-source HRRS images. For performance comparison, several object-based land-use classification methods are utilized. The implementation details, comparison methods, and evaluation metrics are introduced in Section 4.1. Section 4.2 presents

the experimental results of Gaofen-2 (GF-2) images. Section 4.3 tests the transferability of our algorithm on multi-source images.

## 4.1 Experimental setup

### 4.1.1 Pre-processing

For pre-processing, we first remove the near-infrared band of GF-2 images and then re-quantize the responses of the green, red, and blue bands to 8-bit. Since we only utilize the visible spectrum, our algorithm and models can be applied to RS data that have only visible spectrum bands. For GF-1 and ZY-3 images, we conduct the same pre-processing. For JL-1 and GE-WH images, we perform no pre-processing. When annotating label masks, we use the lasso tool in Adobe Photoshop to mark the areas of each land-use category in the images.

### 4.1.2 Comparison methods

We compare our algorithm with several object-based classification methods. Specifically, a set of three different features are exploited, including color histogram (CH) [75], gray-level co-occurrence matrix (GLCM) [76], and local binary patterns (LBP) [77]. Moreover, we consider multi-feature fusion strategy, which aggregates the features by normalization and vector concatenation. Random forest (RF) and support vector machine (SVM) are employed as classifiers. And selective search method is used to segment the image into homogeneous objects. Moreover, we conduct experiments with eCognition, which is a professional and efficient software for RS image analysis.

The parameters of the comparison methods are set to the optimal values. The filter size is set to  $7 \times 7$  pixels for CH and GLCM. And for LBP, the filter size is  $5 \times 5$  pixels. The number of trees for RF is 500. The kernel function of SVM is linear kernel. The initial segmentation size is set to 400 for selective search. We train and test RF and SVM classifiers on the same target imageries. In each image, each category provides 400 training samples.

### 4.1.3 Evaluation metrics

In order to evaluate our algorithm, we assess the experimental results with Kappa coefficient (Kappa), overall accuracy (OA), and class-specific accuracy. Let  $P_{ab}$  denote the number of pixels of class  $a$  predicted to belong to class  $b$ , and let  $t_a = \sum_b P_{ab}$  be the total number of pixels belong to class  $a$ . The metrics are defined as follow:

- *Kappa coefficient*: Kappa is a statistic that measures the agreement between the prediction and the ground truth.

$$Kappa = \frac{P_o - P_c}{1 - P_c} \quad (8)$$

where

$$P_o = \frac{\sum_a P_{aa}}{\sum_a t_a} \quad (9)$$

$$P_c = \frac{\sum_k (\sum_b P_{kb} \cdot \sum_a P_{ak})}{\sum_a t_a \cdot \sum_a t_a} \quad (10)$$

where  $k \in [1, K]$ , and  $K$  is the number of categories.

- *Overall accuracy*: OA is the percentage of correctly classified pixels and all pixels in the entire image.

$$OA = \frac{\sum_a P_{aa}}{\sum_a t_a} \quad (11)$$

- *Class-specific accuracy*: Class-specific accuracy is the percentage of correctly classified pixels for each class.

$$accuracy = \frac{P_{aa}}{t_a} \quad (12)$$

The values of Kappa, OA, and class-specific accuracy are in the range of 0 to 1, and the higher value indicates the better classification performance.

## 4.2 Experiments on Gaofen-2 images

### 4.2.1 Analysis of multi-scale information fusion

To verify the effectiveness of multi-scale information fusion strategy, we compare the classification performance of the single- and multi-scale methods on GID. Image patches of three different sizes are tested:  $56 \times 56$ ,  $112 \times 112$ , and  $224 \times 224$ . For selective search segmentation, the initial segmentation size is set to 400 pixels. The pre-trained ResNet-50 is used directly to classify the target images without fine-tuning. The classification accuracies of different patch sizes are shown in Table 1.

Table 1: Comparison of different patch sample scales.

Patch Size	Kappa	OA (%)	Accuracy (%)				
			built-up	farmland	forest	meadow	waters
$56 \times 56$	0.896	94.94	<b>92.37</b>	94.91	<b>87.98</b>	<b>92.27</b>	82.49
$112 \times 112$	0.873	93.79	86.98	92.52	74.98	75.89	82.18
$224 \times 224$	0.835	91.85	80.54	87.44	70.46	90.85	79.00
Multi-scale	<b>0.913</b>	<b>95.74</b>	87.93	<b>95.38</b>	84.50	80.62	<b>88.36</b>

For single scales, the optimal results are achieved by the smallest patch of size  $56 \times 56$ . This is because our classification method is based on the image patches generated from non-overlapping grid partition, and all pixels in a patch are assigned with the same label. If the patch size is too large, the object details in the patches will be lost. Compared with the best results given by the single-scale approaches, multi-scale information fusion strategy attains the overall highest Kappa and OA of 0.913 and 95.74%, respectively. These results indicate that ground objects in HRRS images show great variations of contextual information in different scales. And combining image information of different scales helps to characterize the spatial distributions of the ground objects and boost the classification performance.

### 4.2.2 Analysis of the segmentation scale

To analyze the influence of the segmentation scale, we test five different initial segmentation sizes for selective search method, including 200, 400, 600, 800, and 1000 pixels. The image patches of size  $56 \times 56$  are used for CNN pre-training and patch-wise classification. We directly utilize the pre-trained ResNet-50 to classify the test images in GID. The experimental results are shown in Table 2.

When the segmentation size is set as 400, the best result is yielded, where Kappa achieves 0.896 and OA reaches 94.94%. In general, for object-based land-use classification, the most suitable segmentation

Table 2: Comparison of different segmentation sizes.

Segmentation Scale	Kappa	OA (%)	Accuracy (%)				
			built-up	farmland	forest	meadow	waters
200	0.890	94.70	<b>92.60</b>	94.02	<b>90.42</b>	<b>94.31</b>	82.63
400	<b>0.896</b>	<b>94.94</b>	92.37	<b>94.91</b>	87.98	92.27	82.49
600	0.886	94.39	90.70	93.88	84.02	93.49	81.23
800	0.870	93.53	87.49	93.13	73.95	89.89	<b>83.18</b>
1000	0.848	92.29	85.34	90.39	69.75	76.34	81.59

scale depends on the resolution of the RS image and the scale of the ground objects. If the image is over-segmented, more noise will be introduced into the classification results, and if the image is under-segmented, the classification map will lose abundant details.

#### 4.2.3 Testing of the transferability of deep models on Gaofen-2 images

To test the effectiveness of the fine-tuning scheme, we compare the performance of CNN models with and without fine-tuning. Two deep models are utilized for classification: 1) ResNet-50 pre-trained on the source domain data, 2) ResNet-50 fine-tuned with FT- $\mathbf{U}_{tg}$ , which are denoted as PT-GID and FT- $\mathbf{U}_{tg}$ , respectively. Multi-scale information aggregation is exploited here, and the initial segmentation size is 400 pixels. The experimental results of our algorithm and the comparison methods are shown in Table 3.

Table 3: Comparison of different land-use classification methods on GID.

Methods	Kappa	OA (%)	Accuracy (%)				
			built-up	farmland	forest	meadow	waters
eCognition	0.564	74.87	76.03	66.89	85.83	85.39	75.34
RF+CH	0.634	79.83	88.74	80.46	31.77	42.54	62.37
RF+GLCM	0.596	75.43	89.13	75.88	51.94	43.90	57.18
RF+LBP	0.666	81.95	75.57	78.37	71.21	68.77	80.62
RF+Fusion	0.728	84.75	89.16	84.16	48.11	71.01	77.16
SVM+CH	0.607	77.69	78.84	76.97	56.31	67.67	65.35
SVM+GLCM	0.549	72.81	86.61	68.89	42.71	68.47	65.09
SVM+LBP	0.475	67.87	59.06	59.24	59.18	59.62	81.83
SVM+Fusion	0.604	77.28	70.15	75.35	69.66	87.00	80.05
PT-GID	<b>0.913</b>	<b>95.74</b>	87.93	<b>95.38</b>	84.50	80.62	<b>88.36</b>
FT- $\mathbf{U}_{tg}$	0.905	95.47	<b>95.19</b>	93.42	<b>87.55</b>	90.35	86.57

It can be seen that PT-GID achieves the highest Kappa and OA of 0.913 and 95.74%, which are slightly higher than the results of FT- $\mathbf{U}_{tg}$ . This experimental phenomenon shows the strong transferability of PT-GID. Although the acquisition location and time are diverse, the same objects have similar spectral response in the images captured by the same sensor (*i.e.* GF-2 satellite). Hence the reliable annotations of the source images can provide sufficient information for classifying the target images. On the contrary, using indeterminate pseudo-labels for fine-tuning may introduce uncertain information into CNN model.

However, among the comparison methods, the optimal results are given by RF+Fusion, yielding Kappa and OA of 0.728 and 84.75%, respectively. Note that, compared with the comparison methods, our algorithm not only obtains higher accuracy, but also does not require the annotation information of the target images.

The results demonstrate the superiority of the proposed algorithm in land-use classification.

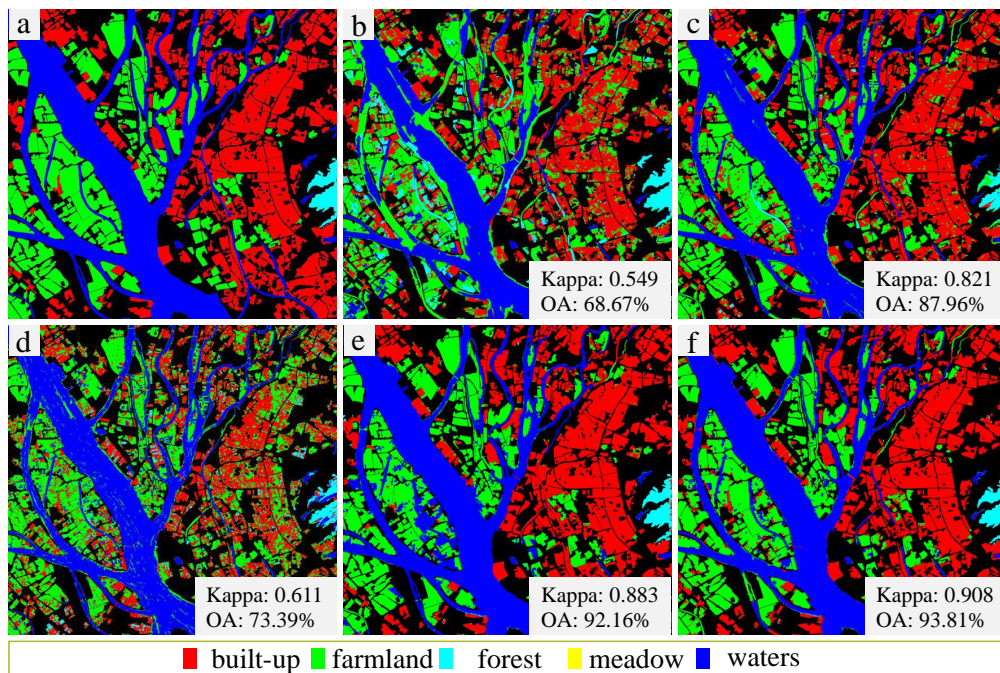


Figure 8: Land-use classification maps of the GF-2 image obtained in Dongguan, Guangdong Province on January 23, 2015. (a) Ground truth. (b)-(f) Results of eCognition, RF+Fusion, SVM+Fusion, PT-GID, and FT- $\mathbf{U}_{tg}$ .

To demonstrate the classification results more intuitively, we display the land-use classification maps. Fig. 8(a) shows the manually labeled ground truth of a GF-2 image obtained in Dongguan, Guangdong Province on January 23, 2015. Fig. 8(b)-(f) are the results generated by eCognition, RF+Fusion, SVM+Fusion, PT-GID, and FT- $\mathbf{U}_{tg}$ . It can be seen that *farmland* is the most difficult class to be recognized in this image. *Built-up* and *farmland* categories are seriously confused by the comparison methods. However, compared to the comparison methods, our algorithm generates the best classification performance for *built-up* and *farmland* categories.

Fig. 9(a) displays the ground truth of a sub image sized  $700 \times 900$  pixels cropped from a GF-2 image, which was acquired in Wuhan, Hubei Province on January 23, 2016. Fig. 9(b)-(f) show the classification results produced by eCognition, RF+Fusion, SVM+Fusion, PT-GID, and FT- $\mathbf{U}_{tg}$ . In Fig. 9, more details can be observed. As shown in Fig. 9(b)-(d), the comparison methods result in a lot of noise in *built-up* category. Whereas, our scheme generates smooth classification maps that close to the ground truth.

### 4.3 Testing of the transferability of deep models on multi-source images

#### 4.3.1 Experiments on Gaofen-1, Jilin-1, and Ziyuan-3 images

This section focuses on validating the effectiveness of the proposed algorithm on images captured by different sensors. PT-GID and FT- $\mathbf{U}_{tg}$  are considered in the experiments. We compare our algorithm with object-based classification methods. The fusion of CH, GLCM, and LBP are used to represent the characteristics of images. The classifiers used are RF and SVM. For RF and SVM, the training samples are randomly selected from GID, where each category contains 3,000 training samples. The annotation information of the target images is not utilized by whether our methods or the comparison methods.



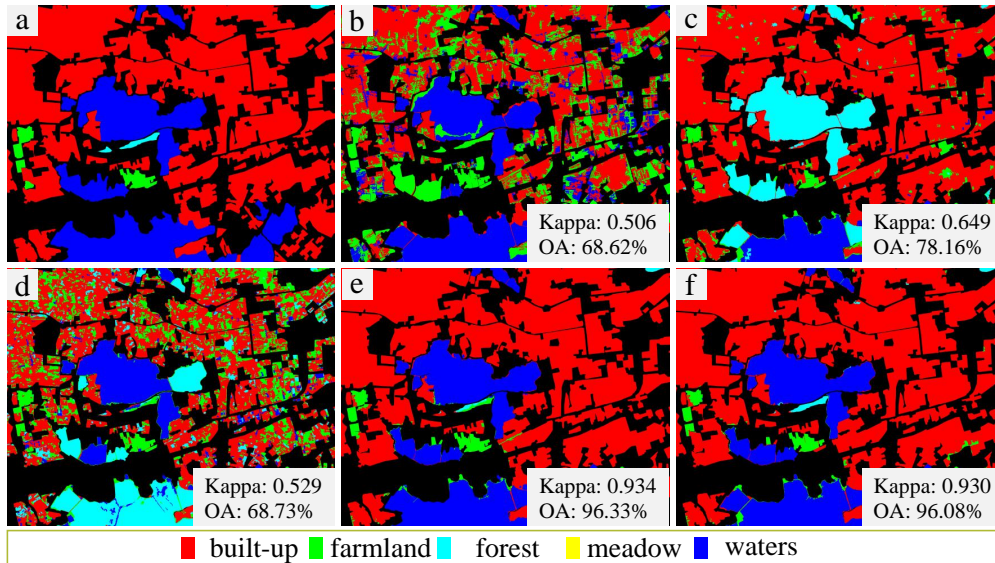


Figure 9: Land-use classification maps of a sub image in the GF-2 acquired in Wuhan, Hubei Province on January 23, 2016. (a) Ground truth. (b)-(f) Results of eCognition, RF+Fusion, SVM+Fusion, PT-GID, and FT- $U_{tg}$ .

The experimental results are shown in Table 4, where OA is used for performance assessment. The accuracy of our algorithm is obviously higher than the comparison methods. For GF-1 (1), GF-1 (2), JL-1 (1), JL-1 (2), ZY-3 (1), and ZY-3 (2), the best OA values are 89.79%, 95.40%, 91.33%, 91.14%, 89.42%, and 95.19%, which are achieved by FT- $U_{tg}$ . These results show that the relevant samples selected from the target domain can strengthen the transferability of CNN models. Therefore, our sample selection and fine-tuning scheme is very effective for multi-source HRRS images.

Table 4: OA (%) of different methods on images captured by different sensors.

	RF+Fusion	SVM+Fusion	PT-GID	FT- $U_{tg}$
GF-1 (1)	49.36	29.89	82.69	<b>89.79</b>
GF-1 (2)	67.79	60.55	92.42	<b>95.40</b>
JL-1 (1)	43.34	14.01	89.44	<b>91.33</b>
JL-1 (2)	84.27	67.63	74.19	<b>91.14</b>
ZY-3 (1)	53.80	51.97	85.71	<b>89.42</b>
ZY-3 (2)	61.34	47.34	92.94	<b>95.19</b>

When our algorithm is applied to images acquired by different sensors, FT- $U_{tg}$  can boost the performance compared to PT-GID. Especially for JL-1 (2), compared with the results of PT-GID, the OA of FT- $U_{tg}$  increases by 16.95%. This experimental phenomenon indicates that, if the spectral response of the target domain and the source domain are similar, the information learned from the source domain samples can benefit the interpretation of the target domain. Conversely, if the spectral response of the target and source domain are very different (*e.g.* obtained by different sensors), the supervision information of the source domain is not reliable for the target domain.

Fig. 10(a)-(b) show JL-1(2) and its corresponding ground truth. Fig. 10(c)-(f) are the results of RF+Fusion, SVM+Fusion, PT-GID, and FT- $U_{tg}$ , respectively. The performance of the comparison methods

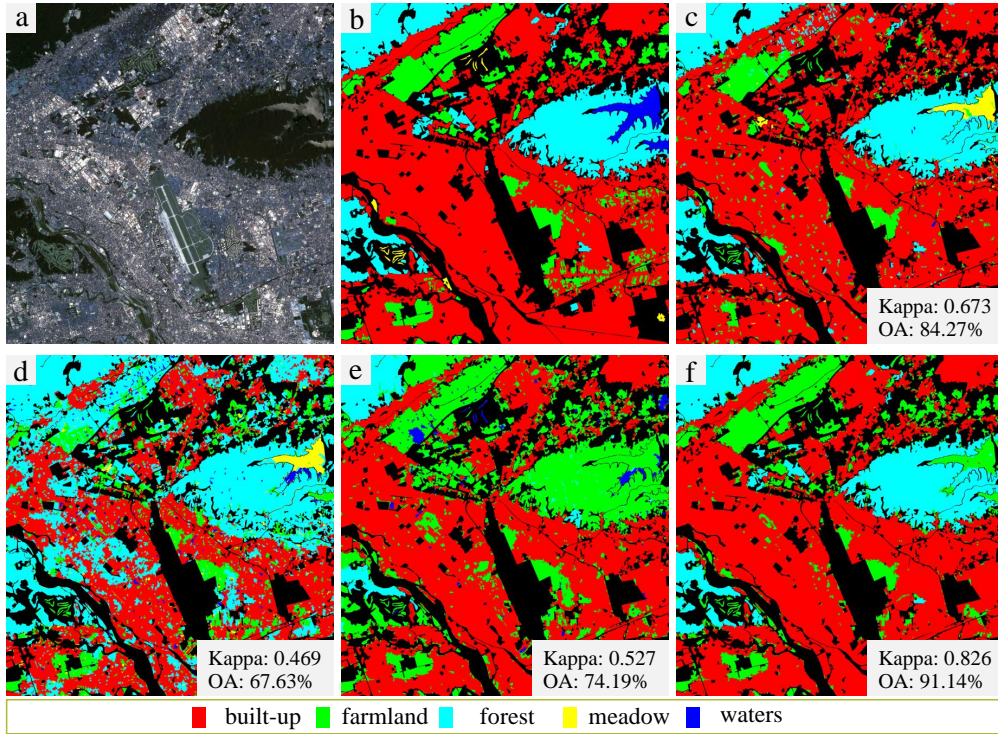


Figure 10: Classification results of JL-1(2). (a) The original image. (b) Ground truth. (c)-(f) Results of RF+Fusion, SVM+Fusion, PT-GID, and FT- $U_{tg}$ .

is unsatisfactory. This is because the distribution of the target domain and the source domain is quite different, and the conventional classifiers do not have sufficient transferability. As shown in Fig. 10(e), *forest* and *farmland* are confused, while in Fig. 10(f), *forest* is correctly classified. The results show that after model fine-tuning, CNN has learnt the distribution of the target domain, which proves that our relevant sample selection scheme can search reliable samples from the target domain.

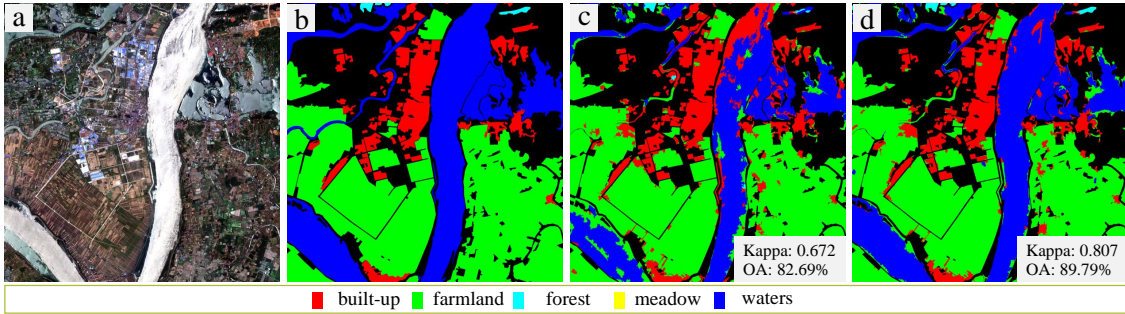


Figure 11: Classification results of a sub image in GF-1 (1). (a) The original sub image. (b) Ground truth. (c)-(d) Results of PT-GID and FT- $U_{tg}$ .

Fig. 11(a)-(b) display a sub image sized  $2000 \times 2000$  pixels cropped from GF-1 (1) and its ground truth. The classification results of PT-GID and FT- $U_{tg}$  are demonstrated in Fig. 11(c)-(d), respectively. These results show the effect of fine-tuning schemes on the classification performance. Compared to Fig. 11(c), less

*built-up* and *farmland* pixels are mistakenly classified as *waters* in Fig. 11(d). These experimental phenomena further validate the robustness and transferability of our approach for diverse HRRS images.

### 4.3.2 Experiments on Google Earth images in Wuhan

In this section, we conduct land-use classification on GE-WH, which is partially annotated for accuracy assessment, as shown in Fig. 12(c). Table 5 displays the classification performance of the different methods. Overall, our method produces the most satisfactory results. The best results of the comparison methods are generated by RF+Fusion, only reaching Kappa and OA value of 0.236 and 35.79%, respectively. However, FT- $U_{tg}$  achieves the overall highest Kappa and OA of 0.924 and 94.56%. Compared to PT-GID, FT- $U_{tg}$  increases Kappa and OA values by 0.205 and 14.24%, respectively.

Table 5: Comparison of different land-use classification methods on GE-WH.

Evaluation Metrics		RF+Fusion	SVM+Fusion	PT-GID	FT- $U_{tg}$
<b>Kappa</b>		0.236	0.012	0.719	<b>0.924</b>
<b>OA (%)</b>		35.79	20.36	80.32	<b>94.56</b>
Accuracy (%)	Built-up	91.41	46.34	53.33	<b>97.68</b>
	Farmland	30.26	0.013	<b>96.41</b>	95.99
	Forest	28.91	66.20	67.51	<b>81.26</b>
	Meadow	<b>17.24</b>	0	3.06	0
	Waters	9.17	4.30	72.07	<b>81.81</b>

Fig. 12(a) shows the original GE-WH. Fig. 12(b) displays the intact classification map produced by FT- $U_{tg}$ . Fig. 12(c)-(d) are the partially annotated label mask and the classification result of FT- $U_{tg}$  in the labeled areas, respectively. It can be seen that some areas in Fig. 12(d) are misclassified, for example, *waters* area in the middle of Wuhan is identified as *farmland*. However, in the absence of labeling information of the target image, our method achieves Kappa and OA values that exceed 90%. These results show that our algorithm has the ability to cope with large-coverage HRRS images. Moreover, they also demonstrate the potential of our algorithm to interface with Google Earth and be practically applied for land-use mapping.

## 5 Conclusion

In this paper, we present a land-use classification algorithm that can be transferred to classify multi-source HRRS images. The proposed algorithm has the following attractive properties: 1) it uses multi-scale contextual information for classification. Hence the spatial distributions of the objects are characterized, and the transferability of classification model for RS images of different resolutions is strengthened. 2) it combines patch-wise classification and hierarchical segmentation. The accurate category and boundary information is therefore simultaneously obtained, and the noise is reduced in the classification map. 3) it automatically selects training samples from the target domain based on the semantic information extracted from deep model. In consequence, it does not require new manually annotating or algorithm adjustment when being applied to multi-source images.

In addition, we constructed a large-scale land-use dataset, *i.e.* GID, with 150 high-resolution GF-2 images. GID has high intra-class diversity and low inter-class separability. It well represents the distribution of land-use categories and can be used to train CNN model specific to RS data. We conduct experiments on multi-source HRRS images, including Gaofen-2 (GF-2) images in GID, coupled with Gaofen-1 (GF-1), Jilin-1 (JL-1), Ziyuan-3 (ZY-3), and Google Earth (GE-WH) images. The proposed algorithm shows encouraging classification performance. In our future research, we hope to improve the automaticity of our method. And

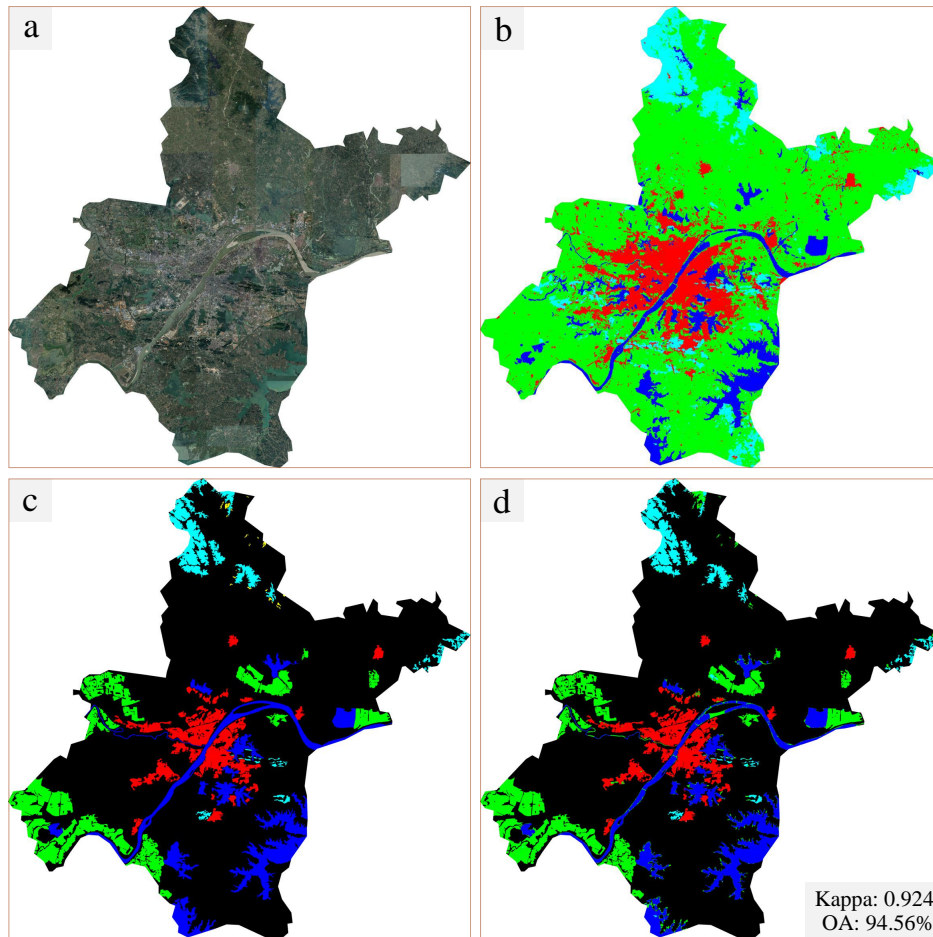


Figure 12: (a) GE-WH image. (b) Classification map produced by FT- $U_{tg}$ . (c) Partially labeled ground truth. (d) Classification result of FT- $U_{tg}$  in the labeled areas.

empirical parameter adjustment is expected to be avoid. In order to benefit researchers, GID have been provided online at <http://captain.whu.edu.cn/GID/>.

## References

- [1] R. Mathieu, C. Freeman, and J. Aryal, "Mapping private gardens in urban areas using object-oriented techniques and very high-resolution satellite imagery," *Landscape and Urban Planning*, vol. 81, no. 3, pp. 179–192, 2007.
- [2] H. Shi, L. Chen, F.-k. Bi, H. Chen, and Y. Yu, "Accurate urban area detection in remote sensing images," *IEEE Geoscience and Remote Sensing Letters*, vol. 12, no. 9, pp. 1948–1952, 2015.
- [3] A. Ozdarici-Ok, A. O. Ok, and K. Schindler, "Mapping of agricultural crops from single high-resolution multispectral imagesdata-driven smoothing vs. parcel-based smoothing," *Remote Sensing*, vol. 7, no. 5, pp. 5611–5638, 2015.

- [4] C. Zhang and J. M. Kovacs, “The application of small unmanned aerial systems for precision agriculture: a review,” *Precision Agriculture*, vol. 13, no. 6, pp. 693–712, 2012.
- [5] J. P. Ardila, V. A. Tolpekin, W. Bijker, and A. Stein, “Markov random field-based super-resolution mapping for identification of urban trees in vhr images,” *ISPRS J. Photogrammetry and Remote Sensing*, vol. 66, no. 6, pp. 762–775, 2011.
- [6] M. Fauvel, Y. Tarabalka, J. A. Benediktsson, J. Chanussot, and J. C. Tilton, “Advances in spectral-spatial classification of hyperspectral images,” *Proceedings of the IEEE*, vol. 101, no. 3, pp. 652–675, 2013.
- [7] G. Moser, S. B. Serpico, and J. A. Benediktsson, “Land-cover mapping by markov modeling of spatial-contextual information in very-high-resolution remote sensing images,” *Proceedings of the IEEE*, vol. 101, no. 3, pp. 631–651, 2013.
- [8] L. Bruzzone and L. Carlin, “A multilevel context-based system for classification of very high spatial resolution images,” *IEEE Trans. on Geoscience and Remote Sensing*, vol. 44, no. 9, pp. 2587–2600, 2006.
- [9] D. Tuia, C. Persello, and L. Bruzzone, “Domain adaptation for the classification of remote sensing data: An overview of recent advances,” *IEEE Geoscience and Remote Sensing Magazine*, vol. 4, no. 2, pp. 41–57, 2016.
- [10] J. R. Jensen and K. Lulla, “Introductory digital image processing: A remote sensing perspective,” *Geocarto International*, vol. 2, no. 1, pp. 65–65, 1986.
- [11] P. Gong, D. J. Marceau, and P. J. Howarth, “A comparison of spatial feature extraction algorithms for land-use classification with spot hrv data,” *Remote Sensing of Environment*, vol. 40, no. 2, pp. 137–151, 1992.
- [12] P. Casals-Carrasco, S. Kubo, and B. B. Madhavan, “Application of spectral mixture analysis for terrain evaluation studies,” *International Journal of Remote Sensing*, vol. 21, no. 16, pp. 3039–3055, 2000.
- [13] S. Giada, T. De Groeve, D. Ehrlich, and P. Soille, “Information extraction from very high resolution satellite imagery over lukole refugee camp, tanzania,” *International Journal of Remote Sensing*, vol. 24, no. 22, pp. 4251–4266, 2003.
- [14] Y. Tarabalka, J. Chanussot, and J. A. Benediktsson, “Segmentation and classification of hyperspectral images using minimum spanning forest grown from automatically selected markers,” *IEEE Trans. on Systems, Man, and Cybernetics, Part B (Cybernetics)*, vol. 40, no. 5, pp. 1267–1279, 2010.
- [15] Y. Tarabalka, M. Fauvel, J. Chanussot, and J. A. Benediktsson, “Svm-and mrf-based method for accurate classification of hyperspectral images,” *IEEE Geoscience and Remote Sensing Letters*, vol. 7, no. 4, pp. 736–740, 2010.
- [16] Y. Zhong, J. Zhao, and L. Zhang, “A hybrid object-oriented conditional random field classification framework for high spatial resolution remote sensing imagery,” *IEEE Trans. on Geoscience and Remote Sensing*, vol. 52, no. 11, pp. 7023–7037, 2014.
- [17] L. Ma, M. Li, X. Ma, L. Cheng, P. Du, and Y. Liu, “A review of supervised object-based land-cover image classification,” *ISPRS J. Photogrammetry and Remote Sensing*, vol. 130, pp. 277–293, 2017.
- [18] B. Zhao, Y. Zhong, G.-S. Xia, and L. Zhang, “Dirichlet-derived multiple topic scene classification model for high spatial resolution remote sensing imagery,” *IEEE Trans. on Geoscience and Remote Sensing*, vol. 54, no. 4, pp. 2108–2123, 2016.

- [19] Y. Zhong, S. Wu, and B. Zhao, “Scene semantic understanding based on the spatial context relations of multiple objects,” *Remote Sensing*, vol. 9, no. 10, p. 1030, 2017.
- [20] F. Hu, G.-S. Xia, J. Hu, Y. Zhong, and K. Xu, “Fast binary coding for the scene classification of high-resolution remote sensing imagery,” *Remote Sensing*, vol. 8, no. 7, p. 555, 2016.
- [21] H. Yu, W. Yang, G.-S. Xia, and G. Liu, “A color-texture-structure descriptor for high-resolution satellite image classification,” *Remote Sensing*, vol. 8, no. 3, p. 259, 2016.
- [22] W. Shao, W. Yang, and G.-S. Xia, “Extreme value theory-based calibration for the fusion of multiple features in high-resolution satellite scene classification,” *International Journal of Remote Sensing*, vol. 34, no. 23, pp. 8588–8602, 2013.
- [23] F. Hu, G.-S. Xia, and L. Zhang, “Deep sparse representations for land-use scene classification in remote sensing images,” in *IEEE International Conference on Signal Processing*, 2017, pp. 192–197.
- [24] W. Yang, X. Yin, and G.-S. Xia, “Learning high-level features for satellite image classification with limited labeled samples,” *IEEE Trans. on Geoscience and Remote Sensing*, vol. 53, no. 8, pp. 4472–4482, 2015.
- [25] F. Hu, G.-S. Xia, J. Hu, and L. Zhang, “Transferring deep convolutional neural networks for the scene classification of high-resolution remote sensing imagery,” *Remote Sensing*, vol. 7, no. 11, pp. 14680–14707, 2015.
- [26] X. X. Zhu, D. Tuia, L. Mou, G.-S. Xia, L. Zhang, F. Xu, and F. Fraundorfer, “Deep learning in remote sensing: A comprehensive review and list of resources,” *IEEE Geoscience and Remote Sensing Magazine*, vol. 5, no. 4, pp. 8–36, 2017.
- [27] A. Krizhevsky, I. Sutskever, and G. E. Hinton, “Imagenet classification with deep convolutional neural networks,” in *International Conference on Neural Information Processing Systems*, 2012, pp. 1097–1105.
- [28] M. D. Zeiler and R. Fergus, “Visualizing and understanding convolutional networks,” in *European Conference on Computer Vision*. Springer, 2014, pp. 818–833.
- [29] G.-S. Xia, J. Hu, F. Hu, B. Shi, X. Bai, Y. Zhong, L. Zhang, and X. Lu, “Aid: A benchmark data set for performance evaluation of aerial scene classification,” *IEEE Trans. on Geoscience and Remote Sensing*, vol. 55, no. 7, pp. 3965–3981, 2017.
- [30] G.-S. Xia, X. Bai, J. Ding, Z. Zhu, S. Belongie, J. Luo, M. Datcu, M. Pelillo, and L. Zhang, “Dota: A large-scale dataset for object detection in aerial images,” in *IEEE Conference on Computer Vision and Pattern Recognition*, 2018.
- [31] P. Napoletano, “Visual descriptors for content-based retrieval of remote-sensing images,” *International Journal of Remote Sensing*, vol. 39, no. 5, pp. 1343–1376, 2018.
- [32] T.-B. Jiang, G.-S. Xia, Q.-K. Lu, and W.-M. Shen, “Retrieving aerial scene images with learned deep image-sketch features,” *Journal of Computer Science and Technology*, vol. 32, no. 4, pp. 726–737, Jul 2017.
- [33] G. Xia, X. Tong, F. Hu, Y. Zhong, M. Datcu, and L. Zhang, “Exploiting deep features for remote sensing image retrieval: A systematic investigation,” *CoRR*, vol. abs/1707.07321, 2017.
- [34] W. Zhao and S. Du, “Learning multiscale and deep representations for classifying remotely sensed imagery,” *ISPRS J. Photogrammetry and Remote Sensing*, vol. 113, pp. 155–165, 2016.

- [35] W. Zhao, Z. Guo, J. Yue, X. Zhang, and L. Luo, “On combining multiscale deep learning features for the classification of hyperspectral remote sensing imagery,” *International Journal of Remote Sensing*, vol. 36, no. 13, pp. 3368–3379, 2015.
- [36] C. Zhang, X. Pan, H. Li, A. Gardiner, I. Sargent, J. Hare, and P. M. Atkinson, “A hybrid mlp-cnn classifier for very fine resolution remotely sensed image classification,” *ISPRS J. Photogrammetry and Remote Sensing*, vol. 140, pp. 133–144, 2018.
- [37] E. Maggiori, Y. Tarabalka, G. Charpiat, and P. Alliez, “Convolutional neural networks for large-scale remote-sensing image classification,” *IEEE Trans. on Geoscience and Remote Sensing*, vol. 55, no. 2, pp. 645–657, 2017.
- [38] N. Kussul, M. Lavreniuk, S. Skakun, and A. Shelestov, “Deep learning classification of land cover and crop types using remote sensing data,” *IEEE Geoscience and Remote Sensing Letters*, vol. 14, no. 5, pp. 778–782, 2017.
- [39] M. Volpi and D. Tuia, “Dense semantic labeling of subdecimeter resolution images with convolutional neural networks,” *IEEE Trans. on Geoscience and Remote Sensing*, vol. 55, no. 2, pp. 881–893, 2017.
- [40] E. Othman, Y. Bazi, F. Melgani, H. Alhichri, N. Alajlan, and M. Zuair, “Domain adaptation network for cross-scene classification,” *IEEE Trans. on Geoscience and Remote Sensing*, vol. 55, no. 8, pp. 4441–4456, 2017.
- [41] Q. Lu, Y. Ma, and G.-S. Xia, “Active learning for training sample selection in remote sensing image classification using spatial information,” *Remote Sensing Letters*, vol. 8, no. 12, pp. 1210–1219, 2017.
- [42] J. Hu, G.-S. Xia, F. Hu, and L. Zhang, “A comparative study of sampling analysis in the scene classification of optical high-spatial resolution remote sensing imagery,” *Remote Sensing*, vol. 7, no. 11, pp. 14988–15013, 2015.
- [43] S. Chakraborty, V. Balasubramanian, Q. Sun, S. Panchanathan, and J. Ye, “Active batch selection via convex relaxations with guaranteed solution bounds,” *IEEE Trans. on Pattern Analysis and Machine Intelligence*, vol. 37, no. 10, pp. 1945–1958, 2015.
- [44] M. Gerke, F. Rottensteiner, J. D. Wegner, and G. Sohn, “Isprs semantic labeling contest,” in *Photogrammetric Computer Vision*. <http://www2.isprs.org/commissions/comm3/wg4/semantic-labeling.html>, 2014.
- [45] E. Maggiori, Y. Tarabalka, G. Charpiat, and P. Alliez, “Can semantic labeling methods generalize to any city? the inria aerial image labeling benchmark,” in *IEEE International Symposium on Geoscience and Remote Sensing*, 2017, pp. 3226–3229.
- [46] G. Mattyus, S. Wang, S. Fidler, and R. Urtasun, “Enhancing road maps by parsing aerial images around the world,” in *IEEE International Conference on Computer Vision*, 2015, pp. 1689–1697.
- [47] L. Ma, M. Li, X. Ma, L. Cheng, P. Du, and Y. Liu, “A review of supervised object-based land-cover image classification,” *ISPRS J. Photogrammetry and Remote Sensing*, vol. 130, pp. 277–293, 2017.
- [48] V. Mnih, “Machine learning for aerial image labeling,” Ph.D. dissertation, University of Toronto (Canada), 2013.
- [49] T. Blaschke, “What’s wrong with pixels? some recent developments interfacing remote sensing and gis,” *GeoBIT/GIS*, vol. 6, pp. 12–17, 2001.
- [50] C. Burnett and T. Blaschke, “A multi-scale segmentation/object relationship modelling methodology for landscape analysis,” *Ecological Modelling*, vol. 168, no. 3, pp. 233–249, 2003.

- [51] U. C. Benz, P. Hofmann, G. Willhauck, I. Lingenfelder, and M. Heynen, "Multi-resolution, object-oriented fuzzy analysis of remote sensing data for gis-ready information," *ISPRS J. Photogrammetry and Remote Sensing*, vol. 58, no. 3-4, pp. 239–258, 2004.
- [52] F. Pacifici, M. Chini, and W. J. Emery, "A neural network approach using multi-scale textural metrics from very high-resolution panchromatic imagery for urban land-use classification," *Remote Sensing of Environment*, vol. 113, no. 6, pp. 1276–1292, 2009.
- [53] G. Xia, J. Delon, and Y. Gousseau, "Shape-based invariant texture indexing," *International Journal of Computer Vision*, vol. 88, no. 3, pp. 382–403, 2010.
- [54] G. Xia, G. Liu, X. Bai, and L. Zhang, "Texture characterization using shape co-occurrence patterns," *IEEE Trans. Image Processing*, vol. 26, no. 10, pp. 5005–5018, 2017.
- [55] L. Zhang, X. Huang, B. Huang, and P. Li, "A pixel shape index coupled with spectral information for classification of high spatial resolution remotely sensed imagery," *IEEE Trans. on Geoscience and Remote Sensing*, vol. 44, no. 10, pp. 2950–2961, 2006.
- [56] D. Tuia, F. Ratle, A. Pozdnoukhov, and G. Camps-Valls, "Multisource composite kernels for urban-image classification," *IEEE Geoscience and Remote Sensing Letters*, vol. 7, no. 1, pp. 88–92, 2010.
- [57] G. Xia, W. Yang, J. Delon, Y. Gousseau, H. P. H. Sun, and H. Maitre, "Structural high-resolution satellite image indexing," in *ISPRS TC VII Symposium C 100 Years ISPRS, Vienna, Austria*, 2010.
- [58] T. Blaschke, "Object based image analysis for remote sensing," *ISPRS J. Photogrammetry and Remote Sensing*, vol. 65, no. 1, pp. 2–16, 2010.
- [59] G. Yan, J.-F. Mas, B. Maathuis, Z. Xiangmin, and P. Van Dijk, "Comparison of pixel-based and object-oriented image classification approaches a case study in a coal fire area, wuda, inner mongolia, china," *International Journal of Remote Sensing*, vol. 27, no. 18, pp. 4039–4055, 2006.
- [60] S. W. Myint, P. Gober, A. Brazel, S. Grossman-Clarke, and Q. Weng, "Per-pixel vs. object-based classification of urban land cover extraction using high spatial resolution imagery," *Remote Sensing of Environment*, vol. 115, no. 5, pp. 1145–1161, 2011.
- [61] D. C. Duro, S. E. Franklin, and M. G. Dubé, "A comparison of pixel-based and object-based image analysis with selected machine learning algorithms for the classification of agricultural landscapes using spot-5 hrg imagery," *Remote Sensing of Environment*, vol. 118, pp. 259–272, 2012.
- [62] S. Paisitkriangkrai, J. Sherrah, P. Janney, V.-D. Hengel *et al.*, "Effective semantic pixel labelling with convolutional networks and conditional random fields," in *IEEE Conference on Computer Vision and Pattern Recognition Workshops*, 2015, pp. 36–43.
- [63] N. Audebert, B. Le Saux, and S. Lefevre, "How useful is region-based classification of remote sensing images in a deep learning framework?" in *IEEE International Geoscience and Remote Sensing Symposium*, 2016, pp. 5091–5094.
- [64] S. Paisitkriangkrai, J. Sherrah, P. Janney, and A. van den Hengel, "Semantic labeling of aerial and satellite imagery," *IEEE J. Selected Topics in Applied Earth Observations and Remote Sensing*, vol. 9, no. 7, pp. 2868–2881, 2016.
- [65] E. Maggiori, Y. Tarabalka, G. Charpiat, and P. Alliez, "High-resolution semantic labeling with convolutional neural networks," *arXiv preprint arXiv:1611.01962*, 2016.
- [66] Y. Liu, D. Minh Nguyen, N. Deligiannis, W. Ding, and A. Munteanu, "Hourglass-shapenetwork based semantic segmentation for high resolution aerial imagery," *Remote Sensing*, vol. 9, no. 6, p. 522, 2017.



- [67] X.-Y. Tong, Q. Lu, G.-S. Xia, and L. Zhang, “Large-scale land cover classification in gaofen-2 satellite imagery,” *arXiv preprint arXiv:1806.00901*, 2018.
- [68] K. He, X. Zhang, S. Ren, and J. Sun, “Deep residual learning for image recognition,” in *IEEE Conference on Computer Vision and Pattern Recognition*, 2016, pp. 770–778.
- [69] K. Chatfield, K. Simonyan, A. Vedaldi, and A. Zisserman, “Return of the devil in the details: Delving deep into convolutional nets,” *arXiv preprint arXiv:1405.3531*, 2014.
- [70] K. Simonyan and A. Zisserman, “Very deep convolutional networks for large-scale image recognition,” *arXiv preprint arXiv:1409.1556*, 2014.
- [71] C. Szegedy, W. Liu, Y. Jia, P. Sermanet, S. Reed, D. Anguelov, D. Erhan, V. Vanhoucke, A. Rabinovich *et al.*, “Going deeper with convolutions,” in *IEEE Conference on Computer Vision and Pattern Recognition*, 2015, pp. 1–9.
- [72] Q. Lu, X. Huang, J. Li, and L. Zhang, “A novel mrf-based multifeature fusion for classification of remote sensing images,” *IEEE Geoscience and Remote Sensing Letters*, vol. 13, no. 4, pp. 515–519, 2016.
- [73] J. R. Uijlings, K. E. Van De Sande, T. Gevers, and A. W. Smeulders, “Selective search for object recognition,” *International Journal of Computer Vision*, vol. 104, no. 2, pp. 154–171, 2013.
- [74] P. F. Felzenszwalb and D. P. Huttenlocher, “Efficient graph-based image segmentation,” *International Journal of Computer Vision*, vol. 59, no. 2, pp. 167–181, 2004.
- [75] J. Wang, W.-j. Yang, and R. Acharya, “Color clustering techniques for color-content-based image retrieval from image databases,” in *IEEE International Conference on Multimedia Computing and Systems*, 1997, pp. 442–449.
- [76] R. M. Haralick, K. Shanmugam *et al.*, “Textural features for image classification,” *IEEE Trans. on Systems, Man, and Cybernetics*, no. 6, pp. 610–621, 1973.
- [77] T. Ojala, M. Pietikäinen, and T. Maenpää, “Multiresolution gray-scale and rotation invariant texture classification with local binary patterns,” *IEEE Trans. on Pattern Analysis and Machine Intelligence*, vol. 24, no. 7, pp. 971–987, 2002.